DE GRUYTER Nanotechnology Reviews 2021; 10: 919–932

Research Article

Jiahao Hu, Jie Ding, Jianping Ai, Honglin Li, Shaozhi Li, Qingbo Ma, Lihui Luo, and Xiaoling Xu*

# Room temperature growth of ZnO with highly active exposed facets for photocatalytic application

https://doi.org/10.1515/ntrev-2021-0057
received June 20, 2021; accepted July 16, 2021

**Abstract:** In this article, the flower-like, urchin-like, and rod-like ZnOs were synthesized by a convenient atmospheric hydrothermal method. The crystalline structures, morphologies, exposed crystal faces, and specific surface areas of the as-prepared ZnO samples were analyzed. Rhodamine B (RhB) was used as the simulated pollutant to evaluate the photocatalytic performance of the ZnO nanostructures. The flower-like ZnO prepared by controlled hydrothermal method at room temperature for 2 h displayed highest specific surface area and exposed more high active $\{2\bar{1}\bar{1}0\}$ facets compared to the other two morphologies of ZnO. In addition, within 2 h of the photocatalytic reaction, the flower-like ZnO results in 99.3% degradation of RhB and produces the most hydroxyl radicals ($\dot{}OH$) 47.83 μmol/g and superoxide anions ($\dot{}O_2^-$) 102.78 μmol/g. Due to the existence of oxygen vacancies on the surface of $\{2\bar{1}\bar{1}0\}$ facets, the flower-like ZnO can efficiently catalyze the production of active oxygen, leading to the improvement in the photocatalytic efficiency.

**Keywords:** ZnO, exposed facets, photocatalytic

## 1 Introduction

Semiconductor materials are widely studied by a number of researchers for the significant roles, which are used in sensors [1], photocatalysis [2], reduction of $CO_2$ [3], air purification [4], and other fields. The different morphologies of semiconductor materials show special characteristics and are beneficial to explore novel functions. Common metal oxides such as $TiO_2$ [5], ZnO [6], $SnO_2$ [7], $BiVO_4$ [8], and CuO [9] recently have become research hotspots in many fields. Among them, ZnO, owning various morphologies, good thermal stability, low cost, and biocompatible, has the potential to substitute $TiO_2$ [10] to be used in photocatalysis and antibacterial field [11].

As a semiconductor material with a wide band gap ($E_g = 3.37$ eV) and large exciton binding energy (60 meV), ZnO has been extensively studied in solar cells [12], antibacterial materials [13], photocatalytic degradation of pollutants [14], and catalytic hydrogen production [15]. In recent years, researchers have commonly used many methods such as material recombination [16], morphology control, and doping [17] to enhance various properties of materials. Among them, ZnO with different morphologies prepared by morphology control exhibits a significant effect on their photocatalytic performance. The difference in morphologies not only leads to different specific surface areas and surface energy, but also results in difference in atom arrangement, which affects the activities and defect concentration. So far, the methods for synthesizing ZnO include hydrothermal [18], chemical vapor deposition [19], ion sputtering [20], sol–gel [21], precipitation method [22], *etc.* The exposure of different facets of ZnO can be controlled by using different solvents, adjusting raw material molar ratio, and changing the traction temperature. Through a large number of theoretical calculations, it can be known that the {0001} facets have the highest catalytic activity [23], followed by the $\{2\bar{1}\bar{1}0\}$ facets [24]. However, due to the high surface energy of {0001}, it is difficult to obtain these facets under mild conditions. ZnO preferentially grow along *c*-axis direction. Xu *et al.* [25] proposed that the growth element is easily adsorbed on the (0001) facets by electrostatic interaction with the hydroxide ions in the solution, which can take $\{2\bar{1}\bar{1}0\}$ as the main exposed crystal surface to control the facets to form a flower-like

---

* **Corresponding author: Xiaoling Xu,** Key Laboratory of Advanced Technologies of Materials (Ministry of Education), School of Materials Science and Engineering, Southwest Jiaotong University, Chengdu 610031, China, e-mail: xiaolingxu@swjtu.edu.cn
**Jiahao Hu, Jie Ding, Jianping Ai, Honglin Li, Shaozhi Li, Qingbo Ma, Lihui Luo:** Key Laboratory of Advanced Technologies of Materials (Ministry of Education), School of Materials Science and Engineering, Southwest Jiaotong University, Chengdu 610031, China

structure. Chen *et al.* [26] used mixed solvents (ethanol and water) to regulate the self-assembly of ZnO crystals and found that stacking along the direction of the [0001] facets has an important regulatory effect. A diol composed of two hydroxyl groups at both ends can be effectively attached to the (0001) facets of the ZnO crystal. This interaction inhibits the preferential growth of ZnO crystals, leading to different orientations of surface morphology [27]. Therefore, methods for preparing ZnO such as vapor deposition, ion sputtering, and crystal assisted methods are not only costly, but also have a complicated process. Furthermore, the use of capping agents and organic additives can probably selectively control the exposed crystal faces of ZnO. But these agents are toxic or corrosive. Therefore, there are few reports on the photocatalytic performance of ZnO with high active exposed crystal faces prepared by an efficient, environmentally friendly, and simple process.

In this article, a mild condition for preparing the highly active ZnO by atmospheric hydrothermal method, without any surfactants, templates, and organic solvents, is reported. The structure of ZnO could be modified by adjusting the molar ratio of raw materials, reaction time, and temperature. The result shows that the flower-like ZnO prepared by hydrothermal method under room temperature exhibits obvious advantage for the photocatalytic performance over the other two kinds of ZnO under simulated sunlight. Due to the different exposed facets of ZnO, this study proposes that the exposed $\{2\bar{1}\bar{1}0\}$ facets of ZnO have a high concentration of oxygen vacancies and outstanding ability to catalyze the production of active oxygen, showing highly efficient photocatalytic performance. The growth principle of flower-like ZnO and the mechanism of high photocatalysis are shown in Figure 1.

# 2 Experimental methods

## 2.1 Materials

Zinc nitrate hexahydrate ($Zn(NO_3)_2{\cdot}6H_2O$), nitro blue tetrazolium chloride (NBT), terephthalic acid (TA), 2-hydroxyterephthalic acid (2-OH-TA), and hexamethylenetetramine (HMTA, $(CH_2)_6N_4$) were purchased from Aladdin Bio-Chem Technology Co., Ltd. (Shanghai, China). NBT, sodium hydroxide (NaOH), ammonia ($NH_3{\cdot}H_2O$), and rhodamine B (RhB) were purchased from Chengdu Kelong Chemical Co., Ltd., P.R. China. All chemical reagents used in this study were used without any further purification.

## 2.2 Synthesis of ZnO

(1) Flower-like ZnO were synthesized using the room temperature hydrothermal method. 2.23 g of $Zn(NO_3)_2{\cdot}6H_2O$ and 3.00 g of NaOH were dissolved in 150 mL of deionized water followed by adding the NaOH solution into the zinc nitrate solution. The mixed solution was reacted for 2 h under magnetic stirring at room temperature. The corresponding product was washed and centrifuged for several times with deionized water and ethanol, and finally dried in air at 60°C for 12 h.

(2) The preparation of urchin-like ZnO was prepared by the hydrothermal method. Typically, 8.92 g of $Zn(NO_3)_2{\cdot}6H_2O$ and 10.50 g of $NH_3{\cdot}H_2O$ were added into 50 mL of deionized water and 200 mL of deionized water, respectively. Then, ammonia solution was added dropwise to the continuously stirred ZnO solution at a rate of 10 mL/min. The mixture was then reacted at 90°C for 20 h. After reaction, the precipitate was naturally

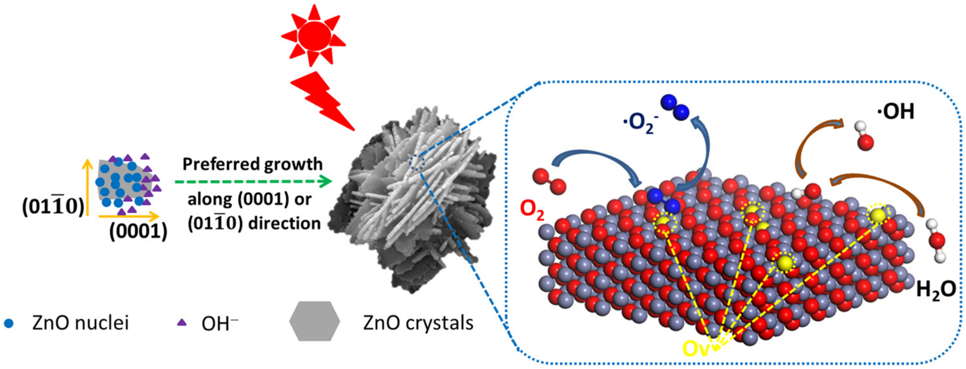

**Figure 1:** Schematic diagram of growth and photocatalysis of flower-like ZnO.

cooled and washed with deionized water and ethanol. Then, it was centrifuged for several times and finally dried in air at 60°C for 12 h.

(3) Rod-like ZnOs were also synthesized by hydrothermal route. Briefly, 8.94 g of $Zn(NO_3)_2{\cdot}6H_2O$ were dissolved in 300 mL of deionized water. 4.20 g of HMTA were added to the above solution. Then, the mixture solution was stirred magnetically at room temperature for 24 h. After stirring, the above solution was transferred into a water bath reacting for 8 h at 90°C. Similarly, the white precipitate obtained after the reaction was washed with water and ethanol followed by centrifuging and then drying in an oven at 60°C for 12 h.

The preparation flow chart of three morphologies of ZnO is shown in Figure 2.

## 2.3 Characterization

The crystal structure of the samples was tested by X-ray diffraction (XRD, Bruker D8 ADVANCE), with CuKα radiation in the $2\theta$ range of 5–85°. The surface morphologies of three kinds of samples were studied by field emission scanning electron microscopy (FE-SEM; Inspect F, FEI, Netherlands), operated at 20.0 kV. More details about the structure of ZnO were studied by transmission electron microscopy (TEM; JSM2100F, JEOL, Japan) and selected-area electron diffraction (SAED) patterns were obtained at an accelerating voltage of 200.0 kV. X-ray photoelectron spectroscopy (XPS) analysis was performed on a Thermo Fisher ESCALAB Xi+ multifunctional imaging electron spectrometer, and the data were corrected by setting the adventitious C 1s peak at a fixed value of 284.8 eV. The Brunauer–Emmett–Teller (BET) special specific surface areas of the samples were detected through measuring the $N_2$ adsorption–desorption isotherms at 77 K using a surface area analyzer (Autosorb iQ, Quantachrome, USA). All samples were studied by ultraviolet-visible (UV-Vis) spectrophotometer (UV-2600, Shimadzu, Japan) to analyze the light absorption ability and detect superoxide radical content. The fluorescence spectrophotometer (Hitachi F-7000) was used to detect the amount of hydroxyl radicals produced by the samples.

## 2.4 Photocatalytic activity tests

Photocatalytic performance of different samples under simulated sunlight were evaluated by degrading RhB at the same temperature using a 150W Xe lamp (XBO 150W/CR OFR, Osram) as the light source. Typically, 40 mg of photocatalysts were dispersed in 40 mL of 10 mg/L RhB solution under continuous stirring. The mixed solution was stirred for 30 min to achieve adsorption–desorption equilibrium at room temperature before irradiation. After photocatalytic reaction for every 20 min, 3 mL of the suspension was taken out followed by centrifuging to remove the catalysts. The UV-Vis spectrophotometer was used to record the

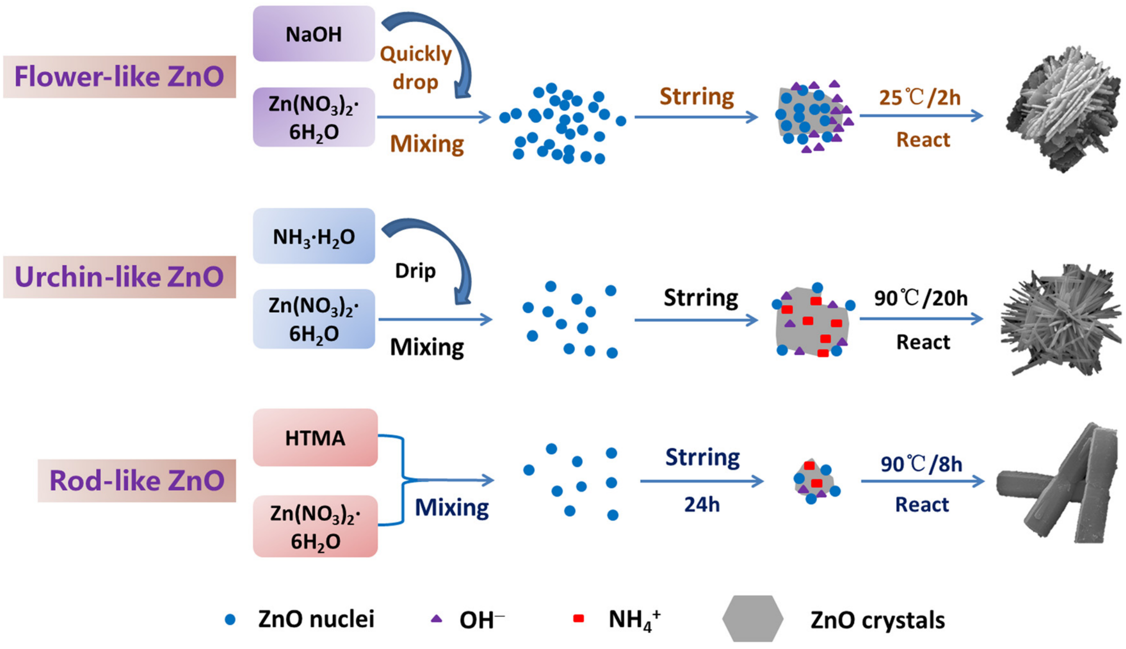

**Figure 2:** Preparation flow chart of ZnO with different morphologies.

concentration change in RhB during the reaction at a wavelength of 553 nm.

## 2.5 Analysis of the hydroxyl radicals

The content of hydroxyl radicals ($^{\cdot}OH$) was mainly detected by using TA as the probe molecule. TA can react with hydroxyl radicals to generate 2-TA-OH which can emit a strong fluorescence signal at around 425 nm under an excitation wavelength of 315 nm. Its production in the solution was detected with the fluorescence spectrophotometer [28,29]. It is known that the PL peak intensity of 2-TA-OH is proportional to the output of hydroxyl radicals. Therefore, through analyzing the PL intensity of 2-OH-TA in the reaction solution, the amount of hydroxyl radicals can be further obtained. This process is similar to the photocatalytic reaction with the difference that the pollutants solution was replaced by TA ($1 \times 10^{-3}$ M) dissolved in NaOH solution ($1 \times 10^{-2}$ M). At different time intervals, the suspension was collected and centrifuged to determine the PL intensity using the fluorescence spectrophotometer with excitation at 315 nm.

## 2.6 Analysis of the superoxide radicals

The production of superoxide radicals ($^{\cdot}O_2^-$) can be measured by using NBT as a probe molecule [30]. NBT has a characteristic absorption peak under ultraviolet visible light at 259 nm. Under the simulated sunlight, NBT can react with $^{\cdot}O_2^-$, generating a blue–purple precipitate. Therefore, the amount of $^{\cdot}O_2^-$ can be calculated by comparing the absorption intensity of NBT at 259 nm in ultraviolet-visible absorption spectrum. This reaction is also similar to the photocatalytic test, using NBT instead of RhB as a degradation product. Put a certain amount of NBT and ZnO into a beaker, collect the suspension for centrifugation within the same reaction time interval, and detect the intensity of NBT by UV-Vis to further calculate the amount of superoxide radicals.

# 3 Results and discussion

## 3.1 Characterization of ZnO

The crystal structure of the prepared samples was studied by XRD as shown in Figure 3. All diffraction peaks are well matched to the wurtzite ZnO (space group $P6_3mc$; JCPDS 36-1451). No other peaks were observed, indicating the successful preparation of pure ZnO crystal. At the same time, the grain size and crystallinity of the samples were calculated by Scherrer's formula, and the results are shown in Table 1. It can be seen from Table 1 that the crystal grain size of flower-like ZnO was 37.1 nm, which is smaller than the urchin-like and rod-like ZnOs. The corresponding crystallinity was only 93.88%, which is also the lowest compared with other samples.

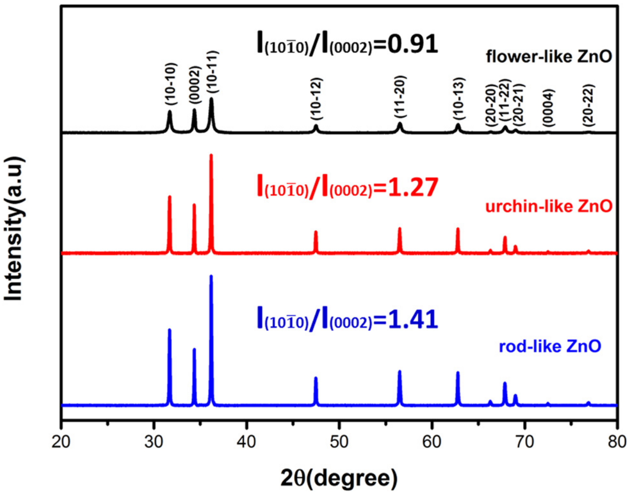

**Figure 3:** XRD patterns of the three samples.

According to Figure 3, the diffraction peaks of the flower-like ZnO were broad and the full width at half maxima were large. Unlike the flower-like ZnO, the diffraction peaks of the urchin-like ZnO and rod-like ZnO were both sharp. Combined with the ZnO crystal data as shown in Table 1, the crystallization and formation of flower-like ZnO was incomplete due to the short reaction time and moderate preparation temperature, leading to the lower crystallinity than the other two ZnOs. In addition, The relative intensity ratio $I_{(10\bar{1}0)}/I_{(0002)}$ reflects the preferred growth direction of the samples. A higher $I_{(10\bar{1}0)}/I_{(0002)}$ demonstrates the existence of a larger crystal face of polar {0001} facets on the sample surface. On the contrary, a lower $I_{(10\bar{1}0)}/I_{(0002)}$ indicates the formation of oriented ZnO along the *c*-axis with [0001] direction, resulting from the interaction between the crystal planes

**Table 1:** The grain size and crystallinity of ZnO with different morphologies

| Sample | Grain size (nm) | Crystallinity (%) |
|---|---|---|
| Flower-like ZnO | 37.1 | 93.88 |
| Urchin-like ZnO | >100 | 98.41 |
| Rod-like ZnO | >100 | 97.71 |

and the ions from the solution during the formation of ZnO. The $I_{(10\bar{1}0)}/I_{(0002)}$ values of the three kinds of ZnO were 0.94, 1.27 and 1.41, respectively, indicating that the exposed {0001} facets proportion was the largest in rod-like ZnO and the smallest in flower-like ZnO. The possible reason could be that the different kinds of alkalis can produce different ions which will selectively be adsorbed on the growth crystal plane of ZnO, thereby changing the preferential growth of the crystal nucleus to the [0001] direction. At last, it will result in the difference in growth direction and different morphologies of ZnO.

After analyzing the crystal structure of the prepared samples, their microscopic morphologies were further studied. As shown in Figure 4, the SEM micrographs of the three different morphologies of ZnO could be observed. It can be seen obviously from Figure 4(a) and (d) that the flower-like ZnOs consisted of multiple slice structures whose thicknesses were 30–60 nm.The size of the flower-like ZnOs were approximately 2–3 µm. Figure 4(b) and (e) illustrates that the urchin-like ZnOs were made up of needle-like structures whose diameters were about 5–6 µm. Figure 4(c) and (f) showed that the rod-like ZnOs are composed of hexagonal prism structures with lengths of 3–4 µm and diameters of 300–600 nm. In combination with Figure 3, it can be concluded that the difference in the growth direction of ZnO can lead to the difference in its morphology.

The exposed facets will change when ZnOs are formed under different conditions. So it is necessary to observe the exposed surface of ZnO by TEM. According to Figure 5, different facets were exposed as the surface of the samples when the morphologies of ZnO were changed. It can be seen from Figure 5(a) that the morphology of ZnO was flower-like shape and Figure 5($a_1$) is the corresponding HRTEM image of this sample. It revealed that the lattice spacing between neighboring lattices is 0.28 and 0.52 nm corresponding to the $\{01\bar{1}0\}$ and {0001} facets, respectively. Meanwhile, the angle between these two crystal planes is 90°. It can also be calculated based on the distance of the diffraction spot in the SAED pattern in Figure 5($a_2$), which implied that flower-like ZnO were orderly grown along the *c*-axis and vertical direction of *c*-axis. In addition, the $I_{(10\bar{1}0)}/I_{(0002)}$ value of flower-like ZnO in Figure 3 was close to 1:1, suggesting that ZnO grows directionally in these two directions and mainly exposed $\{2\bar{1}\bar{1}0\}$ facets.

Figure 5(b)–($b_2$) are the TEM images that exhibit the morphologies and exposed facets of urchin-like ZnO. Figure 5($b_1$) indicated that the clear lattice fringe with

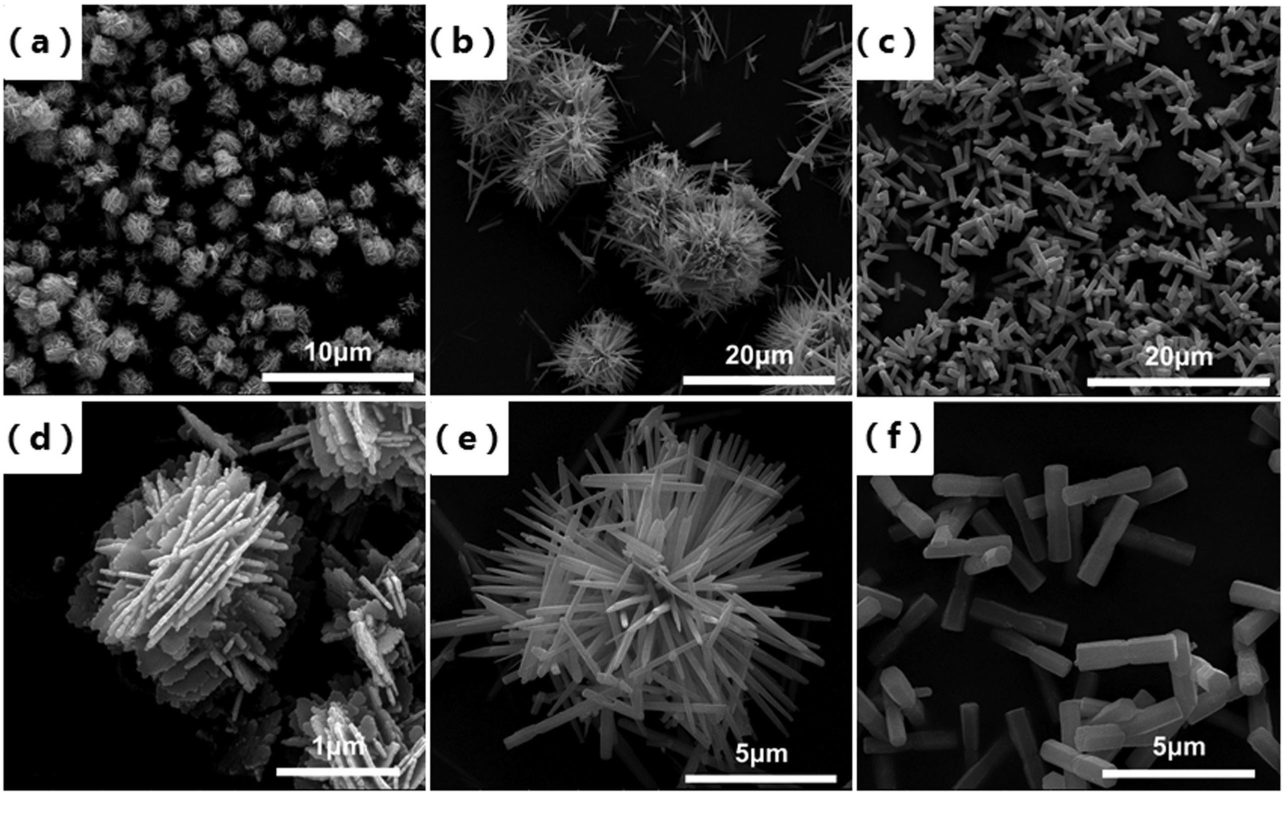

**Figure 4:** SEM images of (a and d) flower-like ZnO, (b and e) sea urchin ZnO, and (c and f) rod-like ZnO.

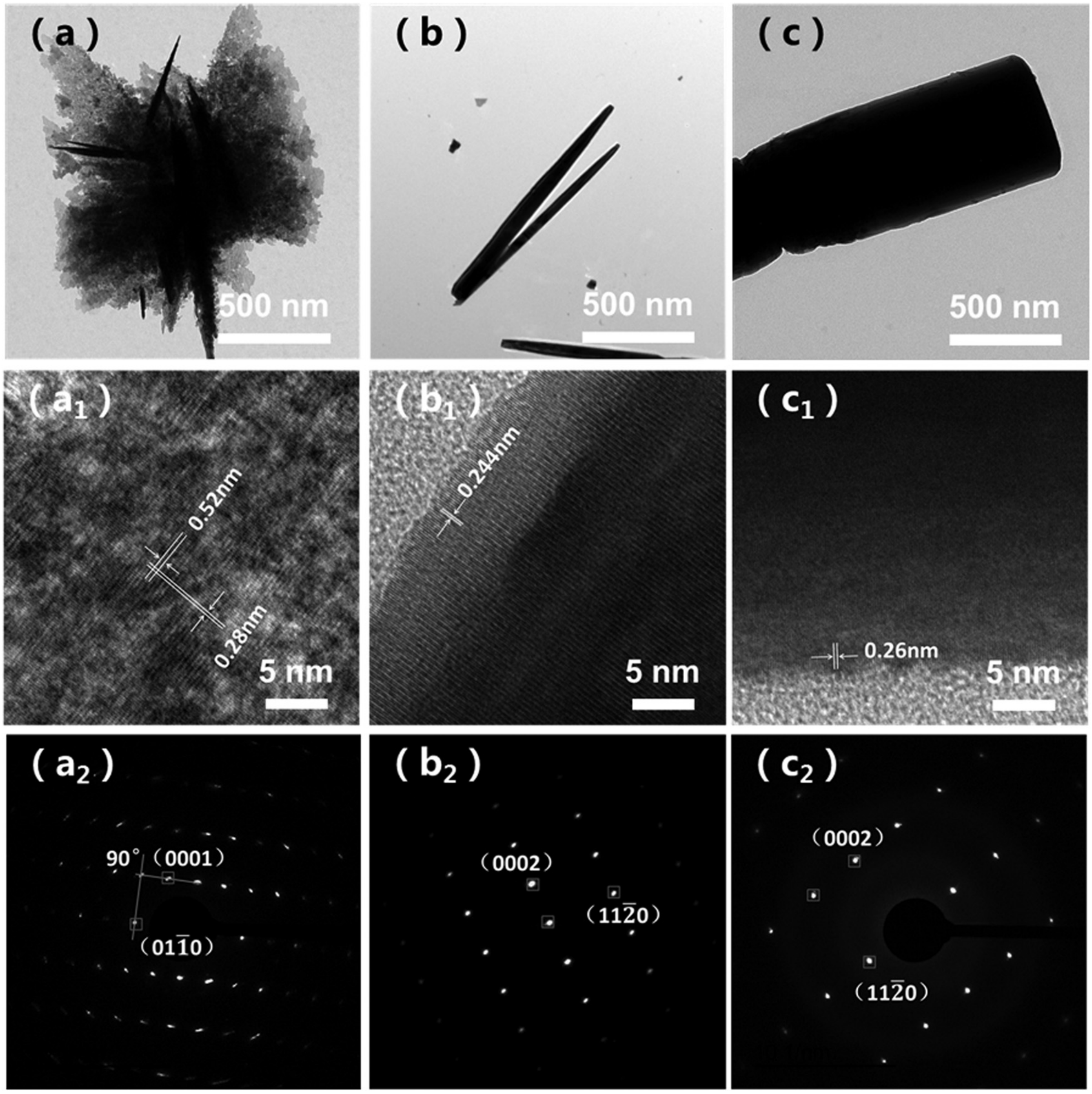

**Figure 5:** TEM and HRTEM images of samples, (a, $a_1$, and $a_2$) flower-like ZnO, (b, $b_1$, and $b_2$) urchin-like ZnO, and (c, $c_1$, and $c_2$) rod-like ZnO.

lattice distance was 0.244 nm which corresponded to the $\{10\bar{1}1\}$ facets. Combined with Figure 3 and SAED pattern, it could be concluded that the growth direction of urchin-like ZnO is preferential along the [0001] direction. Therefore, the main exposed facets of urchin-like ZnO are $\{10\bar{1}0\}$ facets and part of $\{10\bar{1}1\}$ facets [31].

The TEM images of rod-like ZnO are shown in Figure 5(c)–($c_2$). Figure 5($c_1$) exhibits the growth direction of a single rod-like ZnO along the *c*-axis with the lattice fringe of 0.26 nm, corresponding to the distance between the {0001} facets. So that the $\{10\bar{1}0\}$ facets on the side and {0001} facets on the top of rod-like ZnO were exposed. In addition, it is worth to mention that rod-like ZnO has a lower aspect ratio compared with the urchin-like ZnO. Therefore, more {0001} facets are exposed during the formation of this sample. This also corresponds to the relative intensity ratio $I_{(10\bar{1}0)}/I_{(0002)}$ of Figure 3. The rod-like ZnO showed an higher $I_{(10\bar{1}0)}/I_{(0002)}$ ratio compared with urchin-like ZnO, indicating the rod-like ZnO exposes a larger proportion of {0001} facets. The specific surface areas of ZnO will also change due to its different morphologies, which have a certain influence on the number of surface contact substances.

The nitrogen adsorption–desorption isotherms of flower-like ZnO, urchin-like ZnO, and rod-like ZnO are shown in Figure 6. All the samples displayed type-IV isotherms. According to Table 2, the specific surface areas of the samples can be calculated. All three kinds of ZnO had small specific surface areas value (27.0, 9.1 and 4.8 $m^2/g$). The specific surface area of the flower-like ZnO was larger than

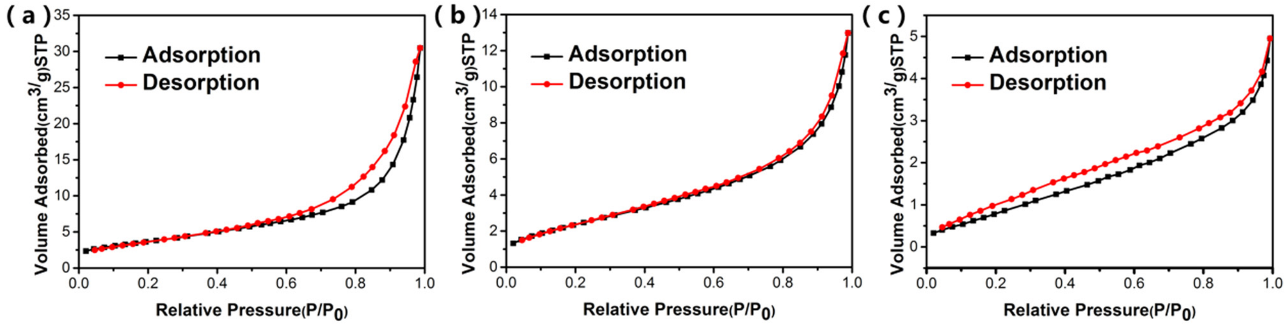

**Figure 6:** $N_2$ adsorption–desorption isotherm of (a) flower-like ZnO, (b) urchin-like ZnO, and (c) rod-like ZnO.

the others. Therefore, the exposure of active surface of flower-like ZnO was larger than the others [32].

## 3.2 Growth mechanism of ZnO with different morphologies

Based on the above analysis, formation mechanisms of ZnO with different morphologies were proposed. The formation of ZnO mainly go through two steps: nucleation and growth. The related reaction chemistry processes are shown as follows:

$$\mathrm{HMTA} + 6H_2O \rightarrow 6HCHO + 4NH_3, \tag{1}$$

$$NH_3 \cdot H_2O \rightarrow NH_4^+ + OH^-, \tag{2}$$

$$Zn^{2+} + 2OH^- \rightarrow Zn(OH)_2 \downarrow \leftrightarrow Zn(OH)_4^{2-}, \tag{3}$$

$$Zn(OH)_4^{2-} \rightarrow ZnO \downarrow + H_2O + 2OH^-. \tag{4}$$

The basic principle was to mix zinc salt with alkali to form growth units, which acted as the nucleus for growth. The growth units finally dehydrated to form ZnO [33]. For flower-like ZnO, the molar ratio $n_{(OH^-)}$:$n_{(zn^{2+})}$ was 10:1. Since the {0001} facets of ZnO have a higher surface energy, the crystal will preferentially grow along the $c$-axis under room temperature [34]. However, with a large amount of $OH^-$ existing in the solution, $OH^-$ will interact with $Zn^{2+}$ under electrostatic Coulomb force since the (0001) facet was full of zinc ions, which would change the surface energy of the (0001) facet. That is why the growth rate in these facets' direction decreased and the growth rate of ZnO toward non-polar facet was enhanced. Therefore, the crystal will grow along the $c$-axis direction and the non-$c$-axis direction at the same time. Finally, the crystals directionally assembled into $\{2\bar{1}\bar{1}0\}$ exposed crystal surface.

**Table 2:** Specific surface areas and oxygen vacancy concentration of ZnO with different morphologies

| Samples | BET ($m^2/g$) | Ov (%) |
|---|---|---|
| Flower-like ZnO | 27.0 | 47.4 |
| Urchin-like ZnO | 9.1 | 42.1 |
| Rod-like ZnO | 4.8 | 44.2 |

When $NH_3{\cdot}H_2O$ was used as the structural regulator for preparing ZnO, there were both $OH^-$ and $NH_4^+$ in the solution, acting as the coordinated ions. Finally, they will be selectively adsorbed on different facets of ZnO [35]. In general, the dominant growth is along $c$-axis direction. Furthermore, due to the adsorption of $NH_4^+$ on the non-polar surface, the particles finally formed needle-shaped ZnO with a small amount of {0001} facets on the top and $\{10\bar{1}0\}$ as well as $\{10\bar{1}1\}$ facets on the side.

For rod-like ZnO, HMTA can decompose into methanol and ammonia which lead to the formation of $OH^-$ and $NH_4^+$. Compared with the direct addition of ammonia, the pH value of adding HMTA is lower. Furthermore, $OH^-$ has a weak effect on the growth process of ZnO, which would result in the growth along the $c$-axis direction. So rod-like particles could be formed [36]. Meanwhile, the exposed facets of ZnO rods are mainly the side $\{10\bar{1}0\}$ and the top {0001} facets.

Therefore, it can be seen that the different morphologies of ZnO comes from the ionization of different alkalis to produce different anions and cations, and the ionized concentrations of ions are also different, so that the interaction between different ions and ZnO is different, thus forming the three specific morphologies.

## 3.3 Photocatalytic performance of ZnO with different morphologies

After successful preparation of the three kinds of ZnO with different exposed facets, the systematic study about photocatalytic properties was carried out. RhB was used as a model pollutant to analyze the catalytic performance. The photocatalytic activities of the three kinds of samples were evaluated by the degradation efficiency of RhB under simulated sunlight irradiation. Figure 7 shows the detailed behavior of RhB photodegradation of flower-like ZnO, urchin-like ZnO, and rod-like ZnO.

Figure 7(a)–(c) shows the UV-visible absorption spectra of RhB during degradation and it can be seen that the characteristic absorption wavelength of RhB is 553 nm. This

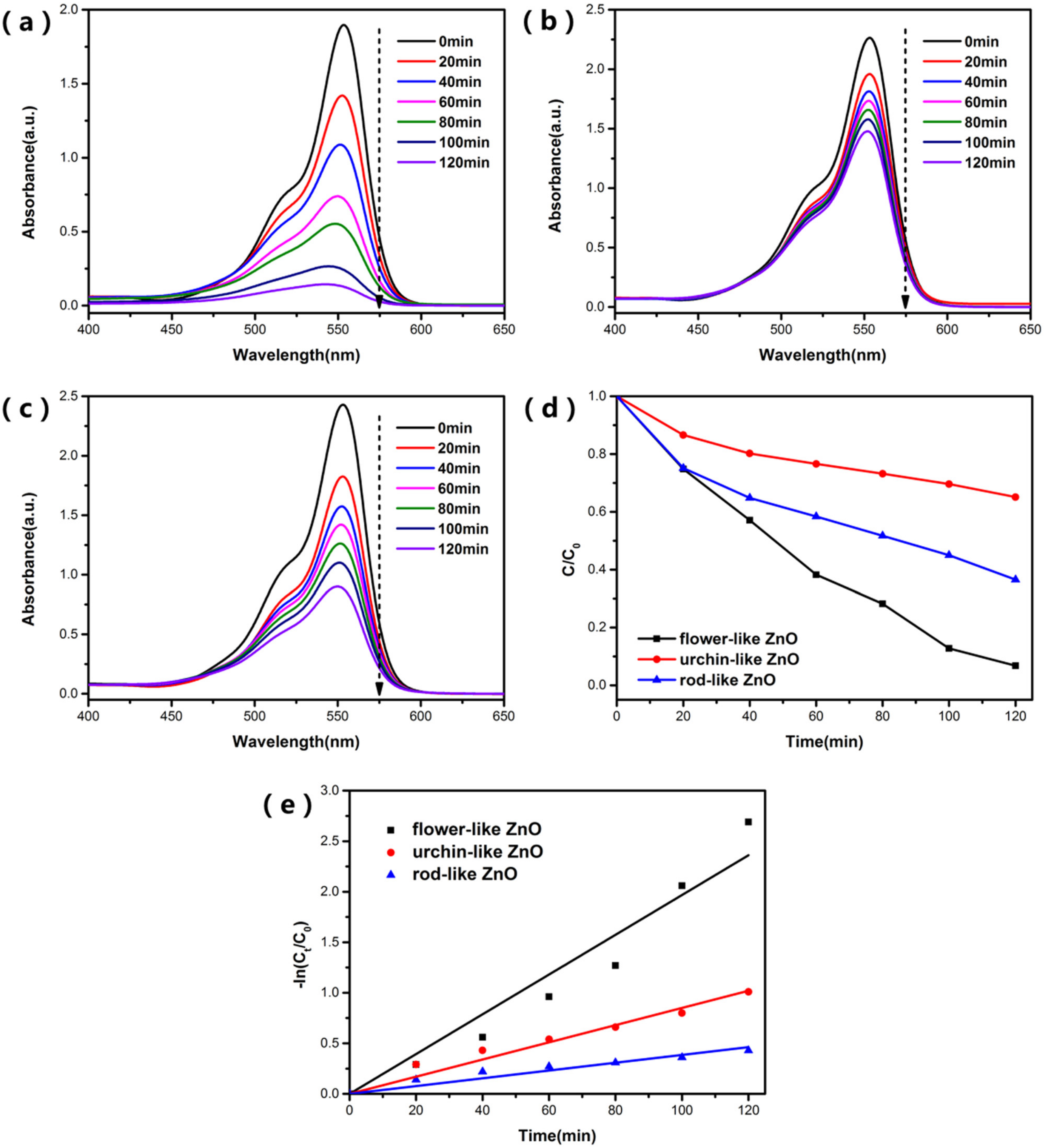

**Figure 7:** The UV-visible absorbance spectra of RhB during degradation by (a) flower-like ZnO, (b) urchin-like ZnO, and (c) rod-like ZnO. (d) Photocatalytic activities of the three samples evaluated by the degradation of RhB under simulated sunlight, and (e) fitted curves with pseudo-first-order kinetic model of samples under simulated sunlight.

characteristic absorption peak of RhB had significant decrease. It proves that flower-like ZnO showed the best photocatalytic performance. After 2 h of simulated sunlight irradiation, the photodegradation efficiencies of RhB were about 99.3, 35.1, and 63.6% for flower-like ZnO, urchin-like ZnO, and rod-like ZnO, respectively. This result does not correspond to the previous BET test results of ZnO. Furthermore, Figure 7(e) represents that the degradation kinetic behaviors of RhB quite fit the pseudo-first-order kinetic model: $\ln (C/C_0) = kt$, where $C$ and $C_0$ are the concentrations of the RhB at time $t$ and at the original time ($t = 0$), respectively. The slope $k$ of these curves represents the apparent reaction rate constant. The bigger degradation rate constant means higher photocatalytic degradation efficiency. The degradation rate constant of the flower-like ZnO is up to 0.0197, which is about 2.3 times that of the urchin-like ZnO and 5.1 times that of the rod-like ZnO. This result also indicates that the flower-like ZnO has a great degradation rate for RhB.

Based on the above results shown in Figure 7, the three types of ZnO have different photocatalytic properties. Besides, there is no correspondence between the difference in photocatalytic performance and the specific surface areas of ZnO, which indicates that the size of the specific surface area of ZnO has a limited effect on its photocatalytic performance.

## 3.4 Photocatalytic mechanism

Since ZnO has different exposed facets, it will result in a difference in the surface oxygen vacancies concentration [37]. Oxygen vacancies will affect the photocatalytic performance of ZnO. Therefore, it is vital to study the surface oxygen vacancies concentration of different samples. Figure 8 shows the high-resolution of Zn and O of the samples. The binding energy of Zn element in ZnO had two peaks at 1,022 and 1,044 eV due to spin splitting. The

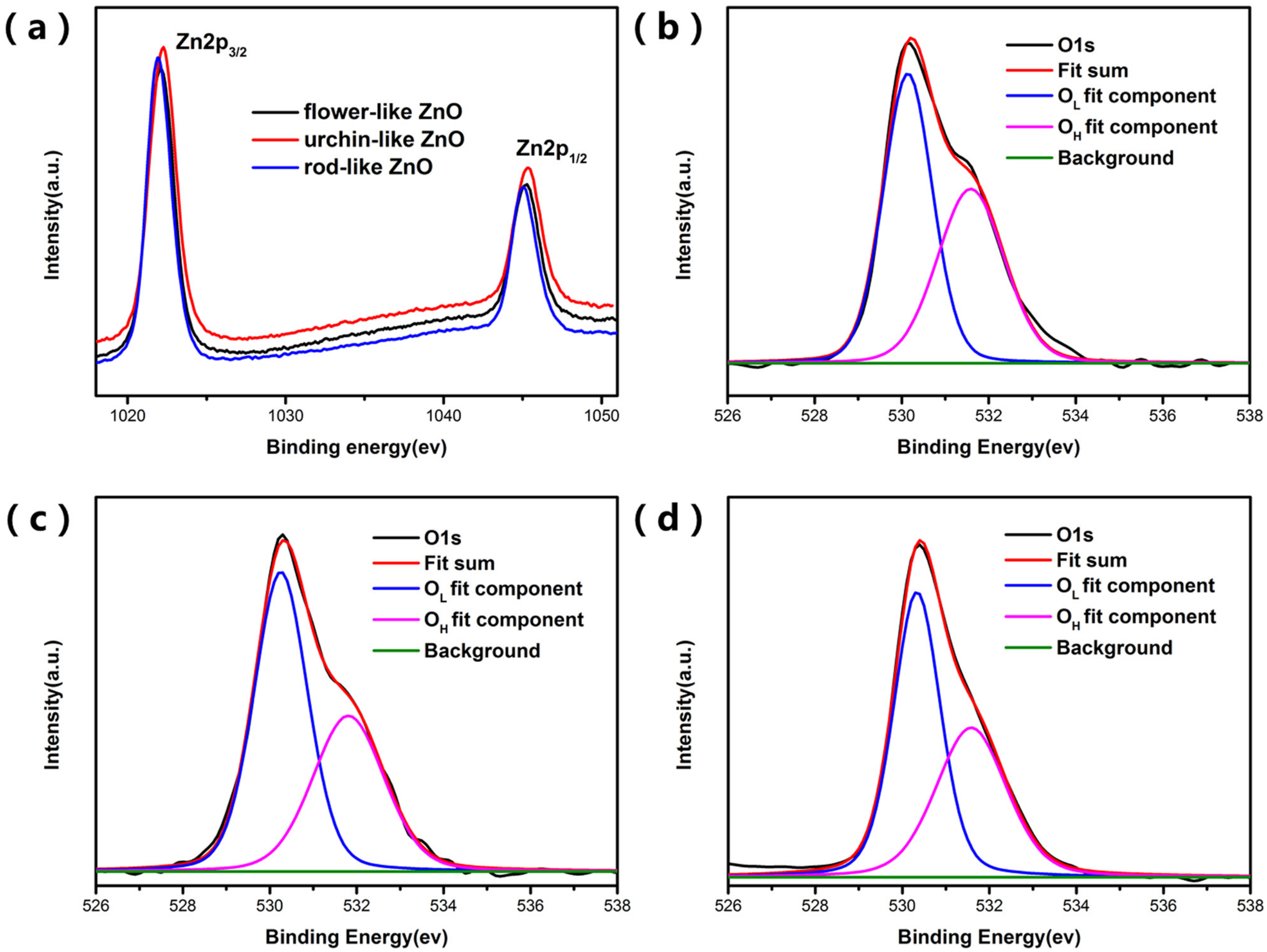

**Figure 8:** XPS analysis of samples showing (a) Zn 2p, (b–d) O 1s spectra of flower-like ZnO, urchin-like ZnO, and rod-like ZnO.

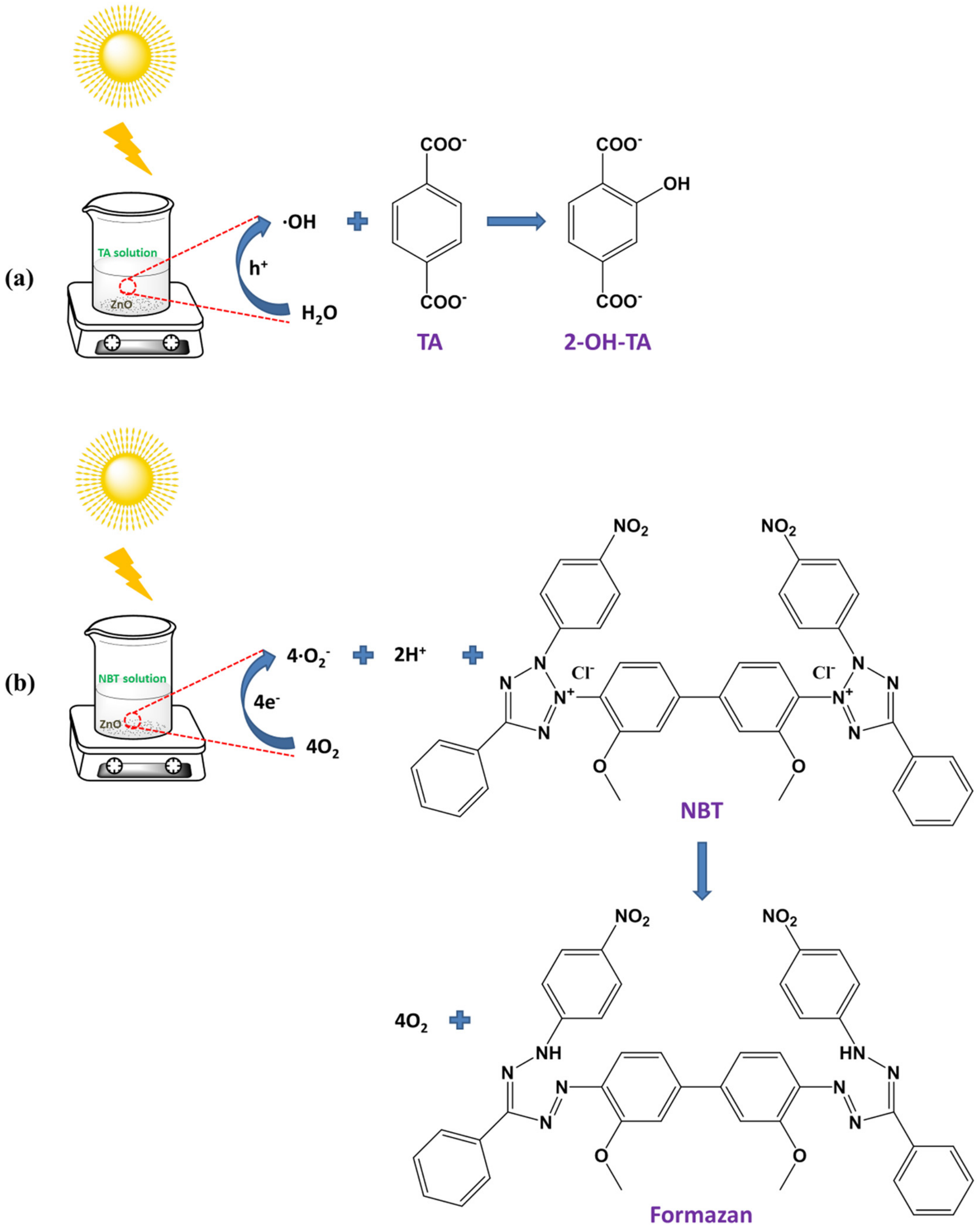

**Figure 9:** Schematic diagram of the principle of ZnO producing active oxygen under simulated sunlight: (a) hydroxyl radical and (b) superoxide anion.

O 1s peak was mainly fitted to two band, as shown in Figure 8(b)–(d). The lattice oxygen ($O_L$) was 530.2 eV which corresponds to the O–Zn bond. The other peak at 531.6 eV was attributed to the binding energy of the ZnO surface to adsorb oxygen from the environment. Because most of the oxygen adsorbed on the surface of ZnO was caused by highly active oxygen vacancies, to a certain extent, the concentration of oxygen vacancies on the surface of ZnO can be expressed by the concentration of adsorbed oxygen on the surface [38]. As displayed in Table 2, the concentration of oxygen vacancies in various ZnO can be calculated by the results of O 1s peak splitting. The results showed that the percentages of oxygen vacancies of these samples were 47.4, 42.1, and 44.2%, respectively. Flower-like ZnO has the most oxygen vacancies content and urchin-like ZnO has the least content.

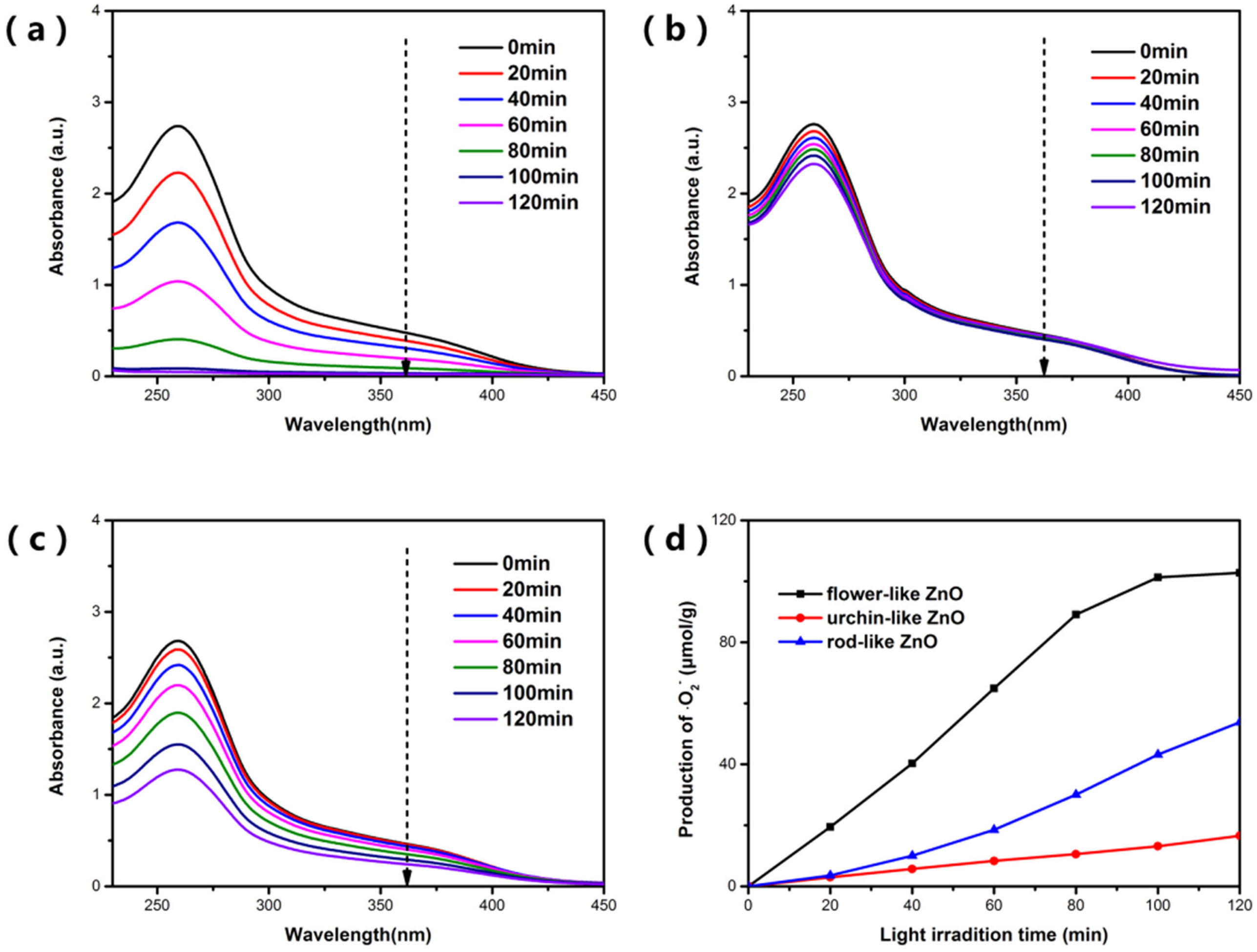

**Figure 10:** UV-Vis absorption spectra of NBT degraded by ZnO with three morphologies of (a–c) flower-like ZnO, urchin-like ZnO, and rod-like ZnO, and (d) the yield of $^{\cdot}O_2^-$ in ZnO suspension under simulated sunlight with time.

Since the photocatalytic performance of ZnO is related to the content of reactive oxygen species produced, the photocatalytic mechanism was further analyzed by quantitatively detecting the amount of $^{\cdot}O_2^-$ and $^{\cdot}OH$ produced by ZnO with different morphologies. The schematic diagram of ZnO generating $^{\cdot}O_2^-$ and $^{\cdot}OH$ under simulated sunlight is shown in Figure 9. The ultraviolet-visible absorption spectrum of degrading NBT obtained by using three kinds of ZnO after simulated sunlight for 2 h is shown in Figure 10. It can be seen that as time passed by, flower-like ZnO had the most obvious degradation effect on NBT, followed by rod-like ZnO and urchin-like ZnO. Therefore, it can be concluded that the $^{\cdot}O_2^-$ content of the samples were 102.78, 53.8, and 16.58 μmol/g. The sample with the highest amount of $^{\cdot}O_2^-$ was the flower-like ZnO. It indicates that flower-like ZnO produces more $^{\cdot}O_2^-$ than the other two ZnO under simulated sunlight. Similarly, the amount of 2-OH-TA produced by the three ZnO in the TA solution was detected by fluorescence spectroscopy in Figure 11. The fluorescence intensity of 2-OH-TA produced by flower-like ZnO was the strongest, and the amount of $^{\cdot}OH$ was 47.83, 24.13, and 10.99 μmol/g. This shows that the flower-like ZnO has the ability to efficiently generate active oxygen compared with others at the same time.

Based on the above analysis, we can know from Figures 10 and 11 that under simulated sunlight, flower-like ZnO with $\{2\bar{1}\bar{1}0\}$ as exposed facets produces the most active substances, which can effectively improve the photocatalytic efficiency. The results of the active oxygen detection and the photocatalysis test were consistent. The possible reason might be that the oxygen vacancies on the different exposed crystal surfaces have different abilities to produce active oxygen. According to the previous work of our research group, the oxygen vacancies in zinc oxide with $\{2\bar{1}\bar{1}0\}$ as exposed crystal planes have a higher capacity for oxygen adsorption and can generate more active oxygen than $\{10\bar{1}0\}$ and other facets [35]. Therefore, flower-like ZnO with high concentration of oxygen vacancies

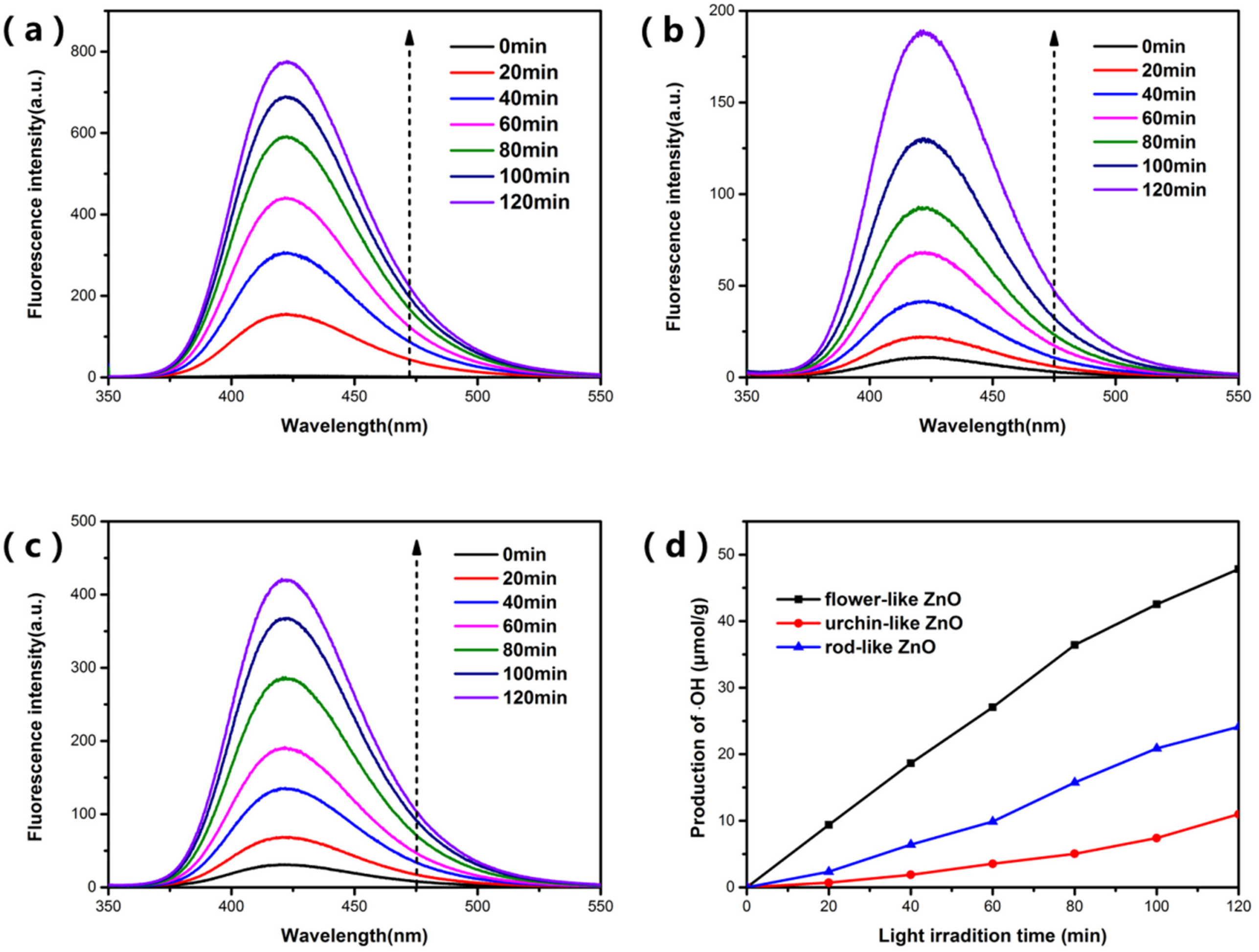

**Figure 11:** Fluorescence spectra of the amount of 2-OH-TA produced by the samples under simulated sunlight over time: (a–c) are the spectra of flower-like ZnO, urchin-like ZnO, and rod-like ZnO, respectively, (d) is the yield of $^{\cdot}$OH in ZnO suspension under simulated sunlight with time.

can produce more active oxygen than the other two samples, exhibiting better catalytic performance.

In short, it can be known that the specific surface area are not the main reasons for the difference in photocatalytic performance. Because ZnOs with different morphologies have different exposed facets, their oxygen vacancy concentration is also different. According to the previous research work of our research group [34], the surface oxygen vacancies of flower-like ZnO with exposed $\{2\bar{1}\bar{1}0\}$ facets compared with the urchin-like and rod-like ZnO with exposed $\{10\bar{1}0\}$ facets can efficiently convert the adsorbed molecular oxygen into $^{\cdot}O_2^-$ in a certain period of time. The photocatalytic mechanism is shown in Figure 12. Therefore, the difference in photocatalytic performance of ZnO with various morphologies are caused by the different abilities in catalyzing the production of active oxygen through their exposed specific facets and surface oxygen vacancies. So, it can be concluded that the specific surface area of ZnO is not the main reason for the difference in photocatalytic performance and the exposed facets of ZnO has a significant influence on this performance.

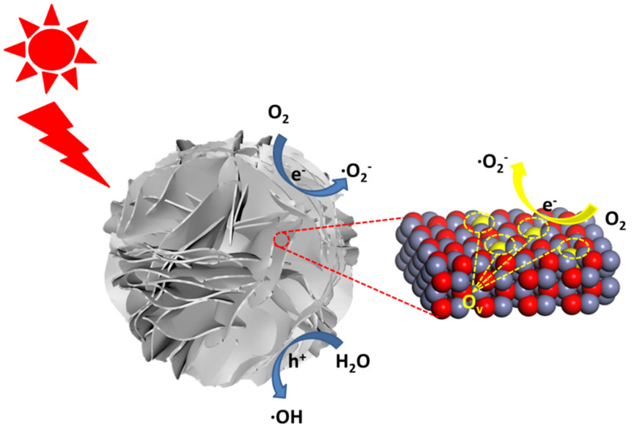

**Figure 12:** The photocatalytic mechanism of flower-like ZnO with exposed $\{2\bar{1}\bar{1}0\}$ facets.

# 4 Conclusion

In summary, ZnO with different morphologies including flower-like ZnO, urchin-like ZnO, and rod-like ZnO were synthesized by an atmospheric hydrothermal method. The electrostatic adsorption between different ions in the solution and the ZnO crystal nucleus had a significant effect on the growth of ZnO, which further affected the formation of various morphologies. Photocatalytic results showed that under the simulated sunlight, the flower-like ZnO exhibited higher photocatalytic activity and produced more active oxygen compared with the other two kinds of ZnO. The excellent photocatalytic performance of flower-like ZnO was attributed to the larger amount of oxygen vacancies on the exposed $\{2\bar{1}\bar{1}0\}$ facets that can catalyze the oxygen and water vapor adsorbed from the environment to generate more active oxygen. The flower-like ZnO with high activity prepared by the room temperature hydrothermal method can be beneficial to the mass production and morphology control of ZnO. It plays an important role in the demand for such semiconductor materials in the fields of photocatalysis, antibacterial, *etc*. For the mechanism study of exposed $\{2\bar{1}\bar{1}0\}$ facets with high catalytic activity, more characterization and theoretical calculations are needed to support these results in order to make this work more complete and detailed.

**Funding information:** This research was financially supported by the National Natural Science Foundation of China (No. 51772251), the Science and Technology Planning Project of Sichuan Province (Nos. 2020ZDZX0008, 2020ZDZX 0005, 2018GZ0431), the Space Station Engineering Aerospace Technology Test Field Project and the Fundamental Research Funds for the Central Universities (No. 2682020XG05).

**Author contributions:** All authors have accepted responsibility for the entire content of this manuscript and approved its submission.

**Conflict of interest:** The authors state no conflict of interest.

# References

[1] Zhang D, Wu X, Han N, Chen Y. Chemical vapor deposition preparation of nanostructured ZnO particles and their gas-sensing properties. J Nanopart Res. 2013;15(4):1–10.

[2] Wang Y, Feng J, Jin L, Li C. Photocatalytic reduction of graphene oxide with cuprous oxide film under UV-vis irradiation. Rev Adv Mater Sci. 2020;59(1):207–14.

[3] Liu X, Ye L, Liu S, Li Y, Ji X. Photocatalytic reduction of $CO_2$ by ZnO micro/nanomaterials with different morphologies and ratios of {0001} facets. Sci Rep. 2016;6(1):1–9.

[4] Pokhum C, Intasanta V, Yaipimai W, Subjalearndee N, Srisitthiratkul C, Pongsorrarith V, et al. A facile and cost-effective method for removal of indoor airborne psychrotrophic bacterial and fungal flora based on silver and zinc oxide nanoparticles decorated on fibrous air filter. Atmos Pollut Res. 2018;9(1):172–7.

[5] Xu H, Reunchan P, Ouyang S, Tong H, Umezawa N, Kako T, et al. Anatase $TiO_2$ single crystals exposed with high-reactive {111} facets toward efficient $H_2$ evolution. Chem Mater. 2013;25(3):405–11.

[6] Jin Y, Long J, Ma X, Zhou T, Zhang Z, Lin H, et al. Synthesis of caged iodine-modified ZnO nanomaterials and study on their visible light photocatalytic antibacterial properties. Appl Catal B Environ. 2019;256:117873.

[7] Wang H, Kalytchuk S, Yang H, He L, Hu C, Teoh WY, et al. Hierarchical growth of $SnO_2$ nanostructured films on FTO substrates: structural defects induced by Sn(II) self-doping and their effects on optical and photoelectrochemical properties. Nanoscale. 2014;6(11):6084–91.

[8] Li R, Zhang F, Wang D, Yang J, Li M, Zhu J, et al. Spatial separation of photogenerated electrons and holes among {010} and {110} crystal facets of $BiVO_4$. Nat Commun. 2013;4(1):1–7.

[9] Cam TS, Vishnievskaia TA, Popkov VI. Catalytic oxidation of CO over $CuO/CeO_2$ nanocomposites synthesized via solution combustion method: effect of fuels. Rev Adv Mater Sci. 2020;59(1):131–43.

[10] Guo Q, Zhou C, Ma Z, Yang X. Fundamentals of $TiO_2$ photocatalysis: concepts, mechanisms, and challenges. Adv Mater. 2019;31(50):1901997.

[11] Luo L, Zhou Y, Xu X, Shi W, Hu J, Li G, et al. Progress in construction of bio-inspired physico-antimicrobial surfaces. Nanotechnol Rev. 2020;9(1):1562–75.

[12] Saleh SM, Soliman AM, Sharaf MA, Kale V, Gadgil B. Influence of solvent in the synthesis of nano-structured ZnO by hydrothermal method and their application in solar-still. J Environ Chem Eng. 2017;5(1):1219–26.

[13] Dejen KD, Zereffa EA, Murthy HCA, Merga A. Synthesis of ZnO and ZnO/PVA nanocomposite using aqueous Moringa oleifeira leaf extract template: antibacterial and electrochemical activities. Rev Adv Mater Sci. 2020;59(1):464–76.

[14] Yang T, Peng J, Zheng Y, He X, Hou Y, Wu L, et al. Enhanced photocatalytic ozonation degradation of organic pollutants by ZnO modified $TiO_2$ nanocomposites. Appl Catal B Environ. 2018;221:223–34.

[15] Núñez J, Fresno F, Platero-Prats AE, Jana P, Fierro JL, Coronado JM, et al. Ga-promoted photocatalytic $H_2$ production over Pt/ZnO nanostructures. ACS Appl Mater Interfaces. 2016;8(36):23729–38.

[16] Zhang C, Fei W, Wang H, Li N, Chen D, Xu Q, et al. p-n Heterojunction of BiOI/ZnO nanorod arrays for piezo-photocatalytic degradation of bisphenol A in water. J Hazard Mater. 2020;399:123109.

[17] Chen A, Zhu H, Wu Y, Chen M, Zhu Y, Gui X, et al. Beryllium-assisted p-type doping for ZnO homojunction light-emitting devices. Adv Funct Mater. 2016;26(21):3696–702.

[18] Xu L, Hu Y-L, Pelligra C, Chen CH, Jin L, Huang H, et al. ZnO with different morphologies synthesized by solvothermal methods for enhanced photocatalytic activity. Chem Mater. 2009;21(13):2875–85.

[19] Liu Z, Liu S, Wu W, Liu CR. The mechanism of controlled integration of ZnO nanowires using pulsed-laser-induced chemical deposition. Nanoscale. 2019;11(6):2617–23.

[20] Nandi R, Major S. The mechanism of growth of ZnO nanorods by reactive sputtering. Appl Surf Sci. 2017;399:305–12.

[21] Mahendraprabhu K, Sharma AS, Elumalai PCO. Sensing performances of YSZ-based sensor attached with sol–gel derived ZnO nanospheres. Sens Actuators B Chem. 2019;283:842–7.

[22] Li S-M, Zhang L-X, Zhu M-Y, Ji GJ, Zhao LX, Yin J, et al. Acetone sensing of ZnO nanosheets synthesized using room-temperature precipitation. Sens Actuators B Chem. 2017;249:611–23.

[23] Sun Y, Chen L, Bao Y, Zhang Y, Wang J, Fu M, et al. The applications of morphology controlled ZnO in catalysis. Catalysts. 2016;6(12):188.

[24] Zhao Y, Cui T, Wu T, Jin C, Qiao R, Qian Y, et al. Polymorphous ZnO nanostructures: zn polar surface-guided size and shape evolution mechanism and enhanced photocatalytic activity. Chem Cat Chem. 2017;9(16):3180–90.

[25] Xu X, Pang H, Zhou Z, Fan X, Hu S, Wang Y. Preparation of multi-interfacial ZnO particles and their growth mechanism. Adv Powder Technol. 2011;22(5):634–8.

[26] Chen X, Song X, Qiao W, Zhang X, Sun Y, Xu X, et al. Solvent-directed and anion-modulated self-assemblies of nanoparticles: a case of ZnO. Cryst Eng Comm. 2016;18(47):9139–51.

[27] Rezapour M, Talebian N. Comparison of structural, optical properties and photocatalytic activity of ZnO with different morphologies: effect of synthesis methods and reaction media. Mater Chem Phys. 2011;129(1–2):249–55.

[28] Wang Q, Guan S, Li B. 2D graphitic-$C_3N_4$ hybridized with 1D flux-grown Na-modified $K_2Ti_6O_{13}$ nanobelts for enhanced simulated sunlight and visible-light photocatalytic performance. Catal Sci Technol. 2017;7(18):4064–78.

[29] Wang J-C, Yao H-C, Fan Z-Y, Zhang L, Wang JS, Zang SQ, et al. Indirect Z-scheme BiOI/g-$C_3N_4$ photocatalysts with enhanced photoreduction $CO_2$ activity under visible light irradiation. ACS Appl Mater Interfaces. 2016;8(6):3765–75.

[30] Bajpai V, Baek K-H, Kang S. Antioxidant and free radical scavenging activities of taxoquinone, a diterpenoid isolated from Metasequoia glyptostroboides. South Afr J Botany. 2017;111:93–8.

[31] Huang M, Weng S, Wang B, Hu J, Fu X, Liu P. Various facet tunable ZnO crystals by a scalable solvothermal synthesis and their facet-dependent photocatalytic activities. J Phys Chem C. 2014;118(44):25434–40.

[32] Flores NM, Pal U, Galeazzi R, Sandoval A. Effects of morphology, surface area, and defect content on the photocatalytic dye degradation performance of ZnO nanostructures. RSC Adv. 2014;4(77):41099–110.

[33] Li P, Wei Y, Liu H, Wang X. A simple low-temperature growth of ZnO nanowhiskers directly from aqueous solution containing $Zn(OH)_4^{2-}$ ions. Chem Commun. 2004;24:2856–7.

[34] Qi K, Cheng B, Yu J, Ho W. Review on the improvement of the photocatalytic and antibacterial activities of ZnO. J Alloy Compd. 2017;727:792–820.

[35] Zhou Y, Guo Y, Li J, Wei W, Li D, Luo L, et al. Excellent antibacterial activities in the dark of ZnO nanoflakes with oxygen vacancies on exposed {2110} facets. J Mater Chem A. 2020;8(23):11511–4.

[36] Baruah S, Dutta J. Hydrothermal growth of ZnO nanostructures. Sci Technol Adv Mater. 2009;10(1):013001.

[37] Wang J, Wang Z, Huang B, Ma Y, Liu Y, Qin X, et al. Oxygen vacancy induced band-gap narrowing and enhanced visible light photocatalytic activity of ZnO. ACS Appl Mater Interfaces. 2012;4(8):4024–30.

[38] Tang Y, Zhou H, Zhang K, Ding J, Fan T, Zhang D. Visible-light-active ZnO via oxygen vacancy manipulation for efficient formaldehyde photodegradation. Chem Eng J. 2015;262:260–7.